Coronal Plasma Characterization via Coordinated Infrared and Extreme Ultraviolet Observations of a Total Solar Eclipse

Chad A. Madsen ¹ ©, Jenna E. Samra ¹ ©, Giulio Del Zanna ² ©, and Edward E. DeLuca ¹ ©

Center for Astrophysics, Harvard & Smithsonian, 60 Garden St., Cambridge, MA 02138, USA; cmadsen@cfa.harvard.edu

Department of Applied Mathematics and Theoretical Physics, CMS, University of Cambridge, Wilberforce Road, Cambridge CB3 0WA, UK

Received 2019 January 29; revised 2019 June 11; accepted 2019 June 18; published 2019 July 31

Abstract

We present coordinated coronal observations of the 2017 August 21 total solar eclipse with the Extreme-ultraviolet Imaging Spectrometer (EIS) and the Airborne Infrared Spectrometer (AIR-Spec). These instruments provide an unprecedented view of the solar corona in two disparate wavelength regimes, the extreme ultraviolet (EUV) and the near- to mid-infrared (IR), opening new pathways for characterizing the complex coronal plasma environment. During totality, AIR-Spec sampled coronal IR spectra near the equatorial west limb, detecting strong sources of Mg VIII, S XI, Si IX, and Si X in two passbands encompassing 1.4–4 μ m. We apply an intensity-ratio diagnostic to a strong resonant Fe XII line pair arising from the coordinated EIS observations. This results in a high-resolution map of electron density throughout the shared EIS/AIR-Spec field of view. Electron density measurements allow us to produce a similar map of plasma temperature using emission measure (EM) loci analysis as applied to 27 EIS emission lines, providing temperatures of $10^{6.12} \pm 10^{3.5}$ K along the limb and $10^{6.19} \pm 10^{3.5}$ K at about 100'' outward. Applying EM loci analysis to AIR-Spec IR spectra coadded over two 31'' wide ranges centered at two locations, 30'' and 100'' from the limb, produces temperatures consistent with the EIS data, albeit suffering from moderate uncertainties. Regardless, we demonstrate that EUV spectral data are valuable constraints to coronal IR emission models, and will be powerful supplements for future IR solar observatories, particularly DKIST.

Key words: eclipses - plasmas - Sun: corona - Sun: infrared - Sun: UV radiation - techniques: spectroscopic

1. Introduction

Total solar eclipses, despite their brevity, can provide rich observational data of coronal emission not otherwise detectable under normal conditions. Lunar occultation of the solar disk eliminates much of the continuum background scattered by Earth's atmosphere that typically overwhelms optically thin coronal emission in the visible, infrared (IR), and near-visible ultraviolet (UV).

Eclipse observations of the IR corona began in the mid-20th century when Blackwell (1952) found IR excesses during a 1952 eclipse, supporting the existence of the F-corona. Similar radiometric observations were repeated to both verify models of coronal structure (e.g., Taylor & MacQueen 1964) and verify the existence of transient coronal dust originating from solar-cometary interactions (Mizutani et al. 1984; Lamy et al. 1992; Hodapp et al. 1992; Tollestrup et al. 1994). IR spectroscopic observations of the corona during eclipse totality began with Kurt (1962) who sought to improve upon coronagraph measurements under daylight conditions (Firor & Zirin 1962). Both works provided the first observational confirmations of the forbidden Fe XIII $1.075/1.080 \,\mu m$ line pair, the most intense coronal IR lines with respect to the continuum. This led to several more successful observations of the line pair during later eclipses (Eddy & McKim Malville 1967; Byard & Kissell 1971; Pasachoff & Muzyka 1976; Pasachoff et al. 1978; Bao et al. 2009; Dima et al. 2018), primarily motivated by the electron density diagnostics associated with their intensity ratio (e.g., Singh et al. 2002 and references therein).

With the advancement of IR instrumentation came the identification of more coronal IR lines observed during total solar eclipse events (e.g., Olsen et al. 1971; Kastner 1993; Dima et al. 2018), including Fe XIV 1.27 μ m, Si X 1.43 μ m,

S XI $1.93 \, \mu m$, Al X $2.75 \, \mu m$, and Mg VIII $3.03 \, \mu m$. Instrumental improvements also drove interest in using IR lines as probes of coronal magnetic fields (e.g., Judge 1998) due in large part to the expected resolvability of emission line splitting due to the Zeeman effect (Zeeman 1897) in the IR. This ultimately provided motivation for construction of the Daniel K. Inouye Solar Telecscope (DKIST; Keil et al. 2009; Tritschler et al. 2016), which will provide dedicated ground-based spectroscopic observing in the IR. This investigative approach has the potential to provide a gamut of new physical plasma diagnostics originating from IR emission lines at unprecedented data volumes. However, diagnostics from IR emission lines are not yet well established.

Unlike the IR regime, physical spectroscopic diagnostics are common tools in the extreme ultraviolet (EUV). The totality of these diagnostic techniques is broad and varied, so we only provide a brief and general history of the subject here. See a review by Del Zanna & Mason (2018) for a more thorough introduction. Early theoretical work examined the link between collisionally induced atomic transitions and the local electron density environment, especially concerning ion species of Fe (Pottasch 1963). The development of electron density and temperature diagnostics for plasmas in the EUV accelerated with the groundbreaking spectroheliographic observations by a series of instruments onboard Skylab (Reeves et al. 1972) such as those used for off-limb density measurements by means of C III line ratios (Doschek & Feldman 1977). Sounding rocket observations, such as those performed by the Solar Extremeultraviolet Rocket Telescope and Spectrograph (Neupert et al. 1992), demonstrated the viability of using strong Mg V-IX and Si VIII-X lines in the EUV as both temperature and density diagnostics (e.g., Dwivedi & Gupta 1993; Dwivedi et al. 1998). The advent of dedicated space-based EUV spectroscopy ushered in by instruments such as the Coronal Diagnostics

Spectrometer (Harrison et al. 1995) and Solar Ultraviolet Measurements of Emitted Radiation (SUMER; Wilhelm et al. 1995) onboard the Solar and Heliospheric Observatory (SoHO), and the Extreme-ultraviolet Imaging Spectrometer (EIS; Culhane et al. 2007) onboard Hinode allowed for the refinement of several diagnostic techniques. EUV spectroscopic diagnostics are now viable for a variety of solar phenomena, including: prominences (e.g., Anzer et al. 2007), coronal holes (e.g., Kayshap et al. 2015; Wendeln & Landi 2018), coronal mass ejections (e.g., McIntosh et al. 2010), and plasmas not in thermodynamic equilibrium (e.g., Dzifčáková & Kulinová 2010; Mackovjak et al. 2013). EUV plasma diagnostics applied to solar spectroscopic data also have application to stellar sources and other astrophysical targets (e.g., Monsignori Fossi & Landini 1994). EUV spectroscopic diagnostics are profoundly versatile and robust, providing a benchmark for the expansion of physical diagnostics into other wavelength regimes.

For this work, we draw attention to two varieties of EUV diagnostics. The first comprises electron density estimates based on intensity ratios of resonant line pairs for a single ion species. Of particular interest are diagnostics reliant on Fe XII line pairs (e.g., Feldman 1981; Feldman et al. 1983; Tayal & Henry 1988; Young et al. 2009; Shimizu et al. 2017), which are strong and abundant throughout much of the EUV in both quiescent and active conditions. The second variety consists of temperature diagnostics using emission measure (EM) estimates. Specifically, we consider an estimate known as the EM loci (Landi et al. 2002a, 2002b, 2012), which when applied to lines from several distinct ion species determines whether an observed plasma can be approximated as isothermal and, if so, also determines the characteristic plasma temperature associated with that state.

The goals of this work are two-fold: (1) to determine the viability of coronal IR emission lines for use as physical plasma diagnostics, and (2) to demonstrate the value of coordinated EUV observations as a supplement to IR spectroscopic observations. We achieve these goals by analyzing two spectroscopic data sets from coordinated off-limb observations taken during the 2017 August 21 total solar eclipse. The first data set consists of IR spectra from the Airborne Infrared Spectrometer (AIR-Spec; Samra et al. 2016) and the second is EUV spectra from EIS. Our general methodology consists of applying EM loci temperature diagnostics to both data sets after using the EUV spectra from EIS for electron density measurements.

This paper proceeds as follows: in Section 2, we outline the capabilities of both instruments and describe their respective data sets; Section 3 establishes the theoretical background underpinning our physical diagnostics and details their application to our data sets; in Section 4, we state the results of our diagnostic analysis and discuss their significance; finally, Section 5 summarizes the paper and extrapolates to related future work.

2. Instruments and Observations

This study focuses on two data sets from observations of the equatorial western limb of the Sun during and shortly after the total solar eclipse of 2017 August 21. The two data sets originate from two distinct instruments, each of which provides spectroscopic data in different passbands: AIR-Spec which observes in the IR, and EIS which observes in the EUV. In this

Table 1
AIR-Spec's Target IR Lines for the 2017 August 21 Eclipse

Ion	Wavelength (μm)	Lower State	Upper State
Si X	1.431	$2s^22p^{-2}P_{1/2}$	$2s^22p^{-2}P_{3/2}$
S XI	1.921	$2s^22p^2 {}^3P_0$	$2s^22p^2 {}^3P_1$
Mg VIII	3.028	$2s^22p^2P_{1/2}$	$2s^22p^2P_{3/2}$
Si IX	3.935	$2s^22p^2 {}^3P_0$	$2s^22p^2 {}^3P_1$

section, we provide instrumental and observational context for those two data sets.

2.1. IR Spectra from AIR-Spec

AIR-Spec is a grating spectrometer designed to observe solar eclipses from aircraft. Observing at altitudes near 15 km abates the primary tropospheric source of opacity in the near-IR: absorption from dense vibrorotational telluric bands of water vapor. This permits Earth-based observation of an IR passband ranging between 1 and 4 μ m. The primary goal of AIR-Spec is to observe magnetically sensitive emission lines in this passband, which could pave the way for direct measurements of the coronal magnetic field in future investigations. However, AIR-Spec also provides a unique opportunity to test the diagnostic potential of coronal IR lines, which we establish as the primary goal of this study.

The spectroscopic capabilities of AIR-Spec provide a reliable means of achieving this goal. Its setup features a nonrotating slit approximately 1.5 R_{\odot} in projected length, suitable for coverage of extended coronal emission. A single InSb detector records the incoming spectra in two channels comprising overlapping first-order and second-order spectra. In first order, the passbands cover ranges from 2.83 to 3.07 μ m and 3.75 to 3.98 μ m with a spectral sampling of 2.4 Å pixel⁻¹. In second order, the spectral sampling improves by a factor of two, setting the wavelength bounds at half the first-order values: 1.42–1.54 μ m and 1.87–1.99 μ m. The spectral resolution is about 15 Å in first order and 7.5 Å in second order. The spatial resolution ranges from 11" to 13", and the projected spatial pixel size is 2."3.

The passbands allow for the observation of emission from four forbidden magnetic dipole transitions in the fine structure of heavy metallic ions. These four lines are: Si X 1.43 μ m, S XI 1.92 μ m, Mg VIII 3.03 μ m, and Si IX 3.94 μ m. The measured line wavelengths and associated transitions are summarized in Table 1. All of the lines originate from ground-state fine-structure transitions induced by electron collisions. Fine-structure transitions are expected to occur far more often than resonance transitions starting at large principal quantum numbers, making these four lines a likely source of bright IR emission in the quiet-Sun corona (Judge 1998; Del Zanna & DeLuca 2018).

AIR-Spec's first eclipse observation took place on 2017 August 21 from 14.3 km over western Kentucky, near the location of maximum totality duration. From the National Science Foundation/National Center for Atmospheric Research Gulfstream V, AIR-Spec observed totality for about four minutes, 1.5 minutes longer than an observer directly below at ground level. During this time, the slit sampled coronal emission from four different pointings. The second of these pointings (henceforth referred to as *pointing #2*) provided the IR spectral data used in this work. It sampled about 41 s of data

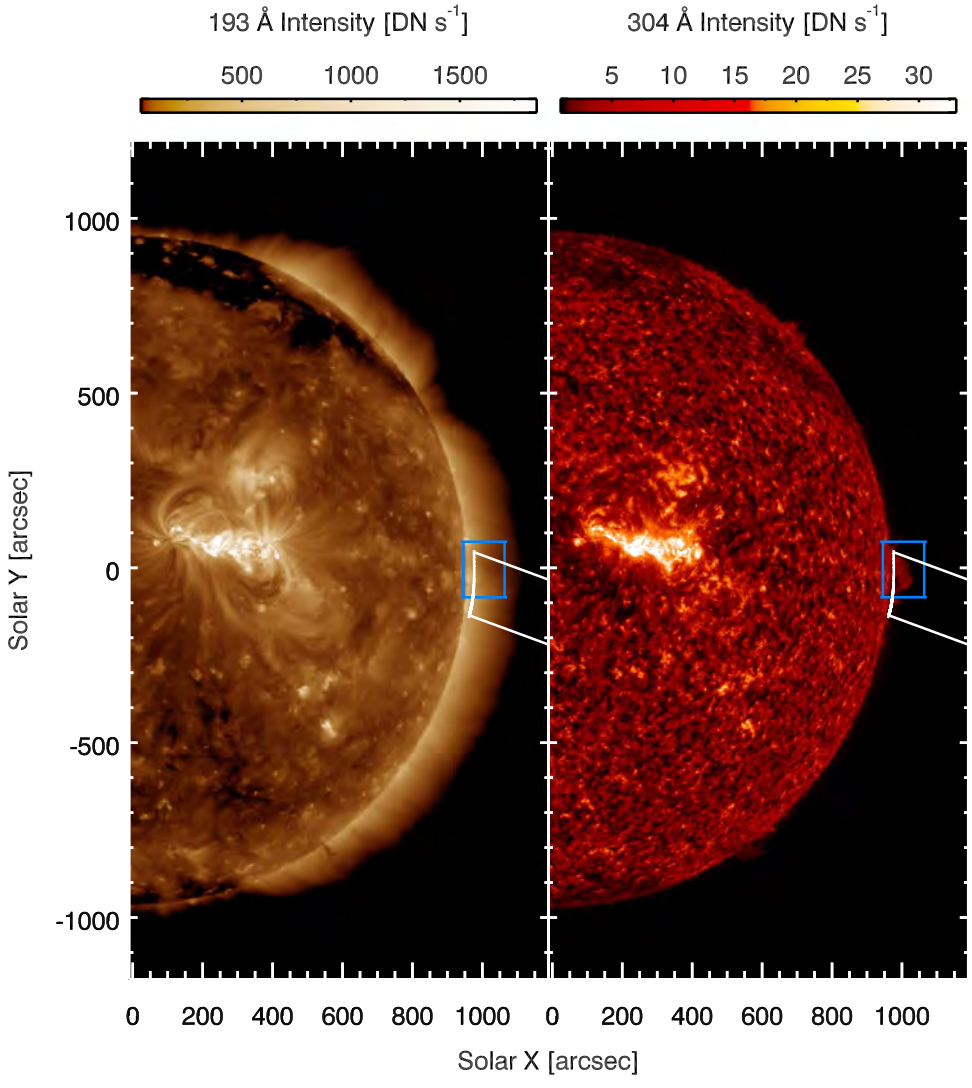


Figure 1. Half-disk AIA 193 Å (left) and AIA 304 Å (right) context images for 2017 August 21 at approximately 21:37 UT depicting the AIR-Spec (white) and EIS (blue) fields of view on the western limb.

from a region near the equatorial western limb occupied by a small prominence and quiet-Sun coronal plasma. The effective field of view (FOV) for pointing #2 is shown on half-disk Solar Dynamics Observatory/Atmospheric Imaging Assembly (SDO/AIA; Lemen et al. 2012) images in Figure 1. Here, we see the slit rotated 21°.2 clockwise from the east—west horizontal. The eastern end of the FOV is a roughly circular arc resting about 25" above the limb; this boundary represents the slit's intersection with the occulting lunar disk. During the 2017 flight, AIR-Spec used an open-loop image stabilization system to compensate for most of the aircraft's motion and to prevent smearing within a single exposure. Some frame-to-frame jitter remained, broadening the sampling range perpendicular to the slit and effectively expanding the FOV's north—south width to about 200".

The data recorded on the day of the eclipse underwent a routine series of calibrations. The radiometric throughput was calibrated in first and second order by exposing the spectrograph to the solar disk in the presence of neutral density $(T=10^{-3})$ and order-isolating filters. A second radiometric calibration was computed by multiplying the slit width, solid angle, and geometric area from the optical design by the

estimated efficiency of each element in the optical train, from the aircraft window to the bandpass filter immediately in front of the detector. The measured throughput is about two times smaller than the modeled throughput, providing a measure of the total uncertainty in the two estimates. Errors were present in both calibrations, and it is not clear which estimate is more accurate. A linear wavelength calibration was performed using the photospheric absorption spectrum to estimate the slope in Å pixel⁻¹ and hydrogen emission lines from the prominence to estimate the wavelength of the first spectral pixel at the time of the observation. To reduce the thermal background and dark current, the spectrometer was passively cooled to below 150 K using liquid nitrogen, a closed-cycle chiller cooled the IR detector to 59 K, and the interface between the spectrometer and IR camera was packed in solid carbon dioxide to reduce its thermal emission onto the detector. The significant residual thermal background, nonuniform in space and nonlinear in time, limited the exposure time to 60 ms and required empirical modeling to remove. For this reason, only the strong first Paschen line (1.88 μ m) from the prominence appeared in the individual frames. However, coadding all 622 frames produced statistically significant detections for all four predicted lines.

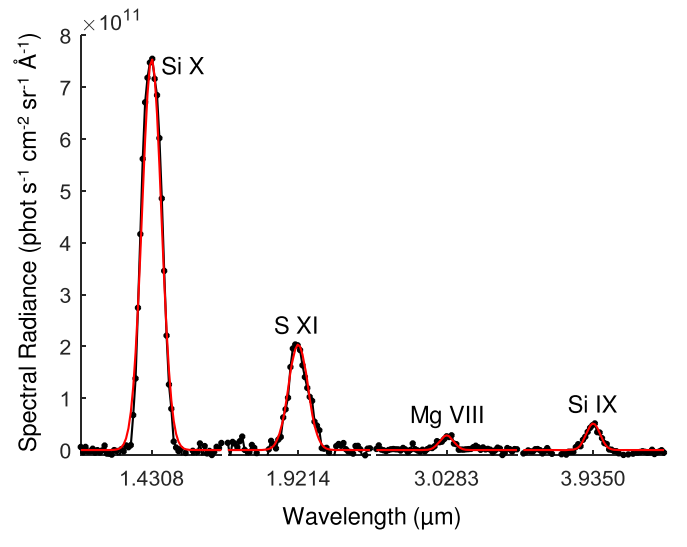


Figure 2. Temporally and spatially averaged AIR-Spec spectral radiance (black dots) at pointing #2. The measurement location is centered 30'' from the solar limb and has a radial extent of 31''. Gaussian fits to the lines are shown in red. Wavelengths are reported in vacuum.

Figure 2 shows the four line profiles measured during pointing #2, averaged in time and over the 35" nearest the lunar limb. AIR-Spec also detected two weak lines: one centered at 2.843 μ m and another centered at 2.853 μ m in air. The former line was originally identified as an Fe IX emission line predicted by Judge (1998) and Del Zanna & DeLuca (2018); however, it was later discovered to be a ghost image of Si X 1.43 μ m produced by the uncoated side of the slit-jaw (Samra et al. 2019). The 2.853 μ m line was determined to be genuine. Its identity remains uncertain, although it stands as a strong candidate for the predicted Fe IX line. Given its questionable identity and weak signal, we did not include this line in our analysis.

2.2. EUV Spectra from EIS

Coordinated observations with EIS onboard Hinode took place approximately two hours after the AIR-Spec observations, starting around 21:36 UT and ending about two hours later at 23:36 UT. EIS pointed approximately 50" above the equatorial western limb, sampling a single west-to-east, 60-step raster with a step size of 2" and a step exposure time of 120 s. Since the vertical pointing of EIS drifts as a function of wavelength, we established 186.8 Å as our pointing and FOV reference. After correcting for spacecraft jitter and coaligning the coordinate system to that of AIA, we found the central pointing at 186.8 Å to be (X, Y) = (1005.5, -4.1) and the slit raster coverage to be 117."9 × 159."0 spanning from at the southeasternmost (945.6, -84.1)corner (1063."6, 74."9) at the northwesternmost corner as shown in Figure 1. Approximately 80% of the EIS FOV area overlaps with the northeasternmost portion of the effective AIR-Spec FOV. AIA cutouts of the EIS FOV are seen in Figure 3. AIA 131, 171, and 304 Å all show evidence of a small prominence extending about 50" from the limb. Additionally, AIA 193, 211 Å, and to a much lesser extent, 94 and 335 Å show two elliptical regions of enhanced intensity rising about 10" off of the limb, one of which is found near Y = -30'' and other occupying the northern limit of the FOV. Overall, the plasma environment appears to be typical of quiet-Sun conditions.

Prioritizing throughput over resolution guided our choice of observing parameters. We used the wider 2" slit, as opposed to the 1" slit, for precisely this purpose. To provide the most detailed diagnostics possible, we used a full readout of EIS's CCD. Consequently, this required a dramatic shrinking of the vertical component of the FOV to accommodate EIS's telemetry limitations. The full-readout mode consists of four broad wavelength windows: two in the short-wavelength regime (166.4 Å \rightarrow 189.2 Å and 189.2 Å \rightarrow 212.0 Å), and two in the long-wavelength regime (245.9 Å \rightarrow 268.7 Å and 268.7 Å \rightarrow 291.4 Å.)

Before analysis, we performed a series of calibrations to transform the level-0 EIS spectral data into level-1 scienceready data, which comprised the following: dark current and bias subtraction, removal of cosmic rays (Pike & Harrison 2000), flagging and removal of hot and warm pixels, an orbital wavelength correction, and a radiometric calibration which converts units of spectral radiance from digital numbers to erg s⁻¹ cm⁻² sr⁻¹ Å⁻¹. For the radiometric calibration, we applied a time-dependent sensitivity decay model (Warren et al. 2014) to the original pre-launch calibration (Lang et al. 2006). The missing pixel values resulting from cosmic ray and warm/hot pixel removal were replaced using a robust hierarchical interpolation scheme implemented through the SolarSoft IDL routine called EIS_REPLACE_MISSING. This particular method was used to minimize the influence of adjacent missing pixels. Interpolated values were derived from neighboring pixels within the same data column, which helps preserve the shape of spectral line profiles. The algorithm replaces an isolated missing pixel value with the average of the pixel values above and below it. However, if one of those neighboring pixel values is missing, then the algorithm will try to find a suitable replacement by taking a weighted average of the nonmissing pixel value and the second-nearest neighbor (or third-nearest neighbor if that too is missing) on the opposite side. If both neighboring pixel values are missing, then the algorithm takes the average of the second-nearest neighbors on either side. If all of these scenarios fail, then the algorithm replaces the missing pixel value with the value assigned to one of its formerly missing neighbors. This process is iterated until all missing values are accounted for; 25.3% of pixels in the EIS data required replacement via this method. Although this technique certainly introduces uncertainty into our analysis, we expect it to not significantly affect our conclusions since the EIS emission lines display a strong signal that remains roughly uniform in the direction parallel to the slit, except for those observed close to the limb which bear influence from the two bright, localized EUV sources seen in Figure 2.

Fourteen frames were rejected from the analysis for various reasons. Five of these coincided with the spacecraft's crossing of the South Atlantic anomaly. Another four were associated with partial or complete dropouts of the CCD readout. The remaining five were associated with an apparent uniform drop in intensity across the detector which could not be explained by accompanying changes to the metadata. For the remainder of this paper, we refer to this incident as the *unexplained dimming*. We also removed a defective row of pixels in the top third of the CCD readout which exhibited anomalously high pixel values.

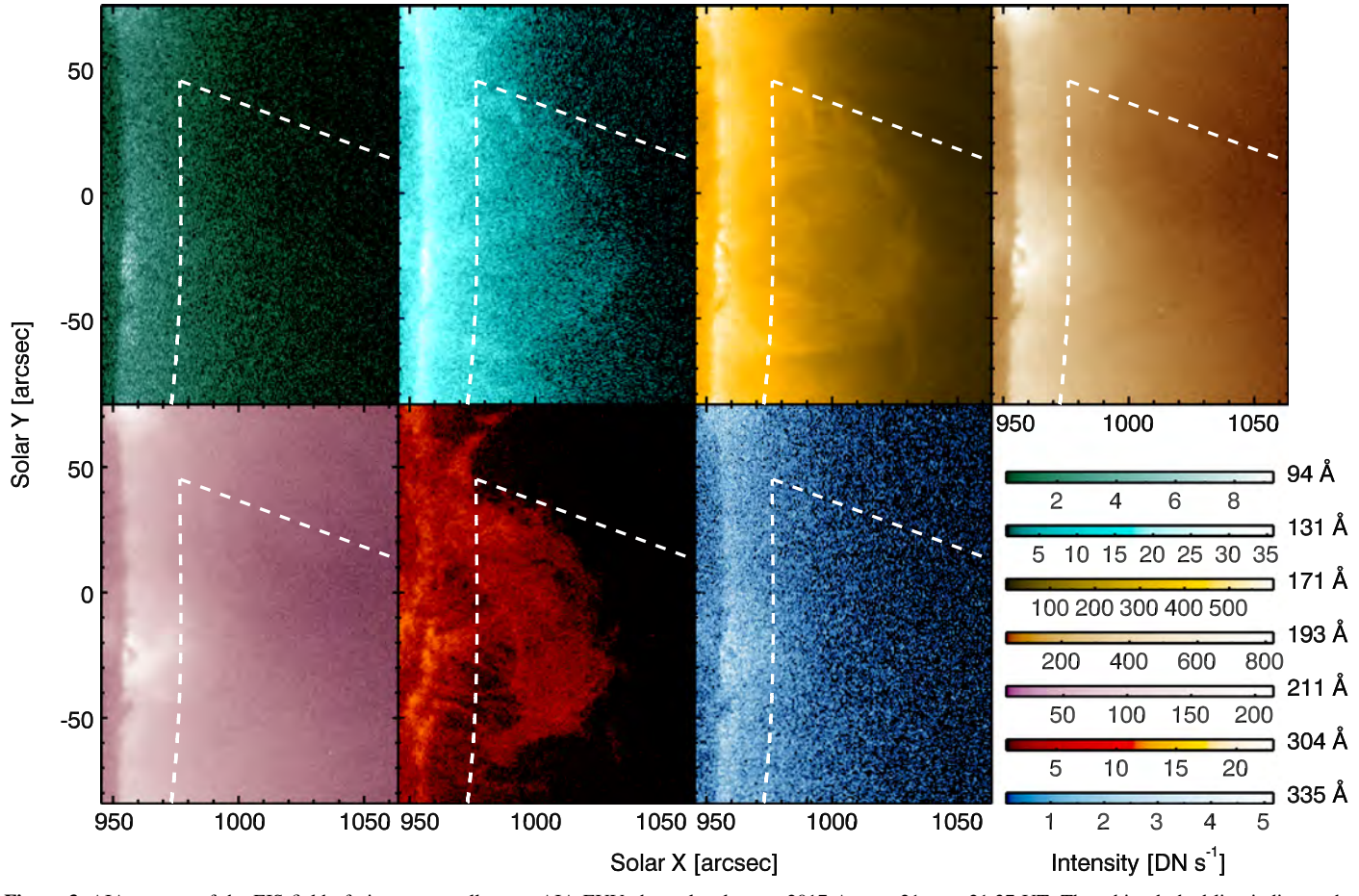


Figure 3. AIA cutouts of the EIS field of view across all seven AIA EUV channels taken on 2017 August 21 near 21:37 UT. The white dashed line indicates the northeastern boundary of the AIR-Spec field of view.

3. Data Analysis

Analysis of the two data sets comprises two distinct steps. First, we use the EIS spectra to produce resolved electron density estimates throughout the EIS FOV. Second, we use the electron density estimates to calculate EM loci for several ion species found in the EIS and AIR-Spec data. The intent of the EM loci analysis is two-fold: (1) to determine whether the coronal plasma volume along each line of sight in the EIS FOV is characteristically isothermal and, if so, (2) to determine the spatial distribution of the associated isothermal temperatures.

3.1. Electron Density Analysis

We determine electron densities using well-established diagnostics applied to resonant Fe XII emission lines (e.g., Pottasch 1963; Feldman 1981; Feldman et al. 1983; Tayal & Henry 1988; Young et al. 2009; Shimizu et al. 2017) found in the EIS spectral window. In particular, we focus on three lines associated with transitions from the $3s^23p^23d$ configuration to the $3s^23p^3$ configuration: 186.85 Å (${}^2F_{5/2} \rightarrow {}^2D_{3/2}$), 186.89 Å (${}^2F_{7/2} \rightarrow {}^2D_{5/2}$), and 192.39 Å (${}^4P_{1/2} \rightarrow {}^4S_{3/2}$). Information about these lines are summarized in Table 2. The former two lines comprise a self-blend which we treat as a single line called Fe XII 186.85/.89 Å for the purposes of this analysis. The diagnostic method used in this work concerns a relationship between intensity ratios of Fe XII emission lines and the electron densities associated with their line-of-sight source volumes. It works by exploiting the efficiency difference by

 Table 2

 EIS EUV Fe XII Lines Used for Electron Density Analysis

Wavelength (Å)	Lower State	Upper State	$A_{\text{lu}} (s^{-1})$
186.854	$3s^23p^3 \ ^2D_{3/2}$	$3s^23p^23d^2F_{5/2}$	1.010×10^{11}
186.887	$3s^23p^3 {}^2D_{5/2}$	$3s^23p^23d^2F_{7/2}$	1.080×10^{11}
192.394	$3s^23p^3 \ ^4S_{3/2}$	$3s^23p^23d^4P_{1/2}$	8.830×10^{10}

which collisional processes populate the upper states of the transitions associated with each line.

We proceed by establishing the basic framework of this diagnostic. For a more detailed review, refer to Del Zanna & Mason (2018). To begin, we find the intensity I at wavelength λ for emission due to a transition from an upper state j to a lower state i within species X at ionization state +m assuming an optically thin plasma:

$$I_{ij}(X^{+m}; \lambda_{ij}) = \frac{1}{4\pi R^2} \int_V \epsilon_{ij}(X^{+m}) dV$$
$$= \frac{h\nu_{ij}}{4\pi R^2} \int_V n_j(X^{+m}) A_{ij}(X^{+m}) dV$$
(1)

where R is the distance from the emission source to the observer, V is the line-of-sight volume of the emission source, $\epsilon_{ij}(X^{+m})$ is the volume emissivity for a transition between states i and j of ion species X at ionization state +m, ν_{ij} is the frequency associated with λ_{ij} , $n_j(X^{+m})$ is the volume number

density of ions of species X in ionization state +m at upper state j within the source volume, and $A_{ij}(X^{+m})$ is the Einstein coefficient for spontaneous emission of transition $j \to i$ for the same ion species (Einstein 1916). Note that our definition of intensity, Equation (1), uses energy units instead of photon units.

 $A_{ij}(X^{+m})$ only depends on the upper and lower states of the transition, so all intensity variation with respect to electron density originates from $n_j(X^{+m})$. However, calculating $n_j(X^{+m})$ is no simple task since we need information on all possible transitions to and from the upper state j within the ion. If we assume that the plasma is in ionization equilibrium and the timescale for electron collisions is much smaller than the observation time, then we can determine $n_j(X^{+m})$ using the principle of detailed balance:

$$n_{j}(X^{+m}) \left[n_{e} \sum_{k \neq j} C_{kj}(X^{+m}) + \sum_{k < j} A_{kj}(X^{+m}) \right]$$

$$= n_{e} \sum_{k \neq j} n_{k}(X^{+m}) C_{jk}(X^{+m}) + \sum_{k > j} n_{k}(X^{+m}) A_{jk}(X^{+m}) \qquad (2)$$

where n_e is the electron number density and $C_{qp}(X^{+m})$ is the rate coefficient for a collisionally induced transition (either excitation or de-excitation) from a state p to some other state q in ion species X^{+m} . According to Equation (2), solving for $n_j(X^{+m})$ requires knowledge of the number densities for every other state in the ion. Assuming there are N_s non-negligible states in the ion, we can apply Equation (2) to each of those states, producing a system of N_s linear equations. To make this set of equations inhomogeneous and thus solvable for $n_j(X^{+m})$, we introduce

$$\sum_{k} n_k(X^{+m}) = n(X^{+m}) \tag{3}$$

where $n(X^{+m})$ is the total volume number density of ion X^{+m} in the source volume, a value that depends on the yet unknown temperature of the plasma. Fortunately, $n(X^{+m})$ cancels when $n_i(X^{+m})$ is taken in ratio with another state density. Coupling this with the assumption that the temperature and density are uniform and constant within the source volume, we can then use Equations (1) and (2) to relate the intensity ratio of two emission lines to the electron density. The functional form of this relationship is that of a ratio of two higher-order polynomials of the electron density, the coefficients of which are composed of A and C values in elementary combinations. The complexity of this relationship is dependent entirely upon the choice of line pair. While any two lines originating from the same species will satisfy our assumptions, only a rare few will provide a simple enough relationship between their intensity ratio and the electron density to be useful for our analysis. In general, we need a line pair that provides the following: (1) a one-to-one relationship between the intensity ratio and the electron density within the domain of typical coronal densities, and (2) a wide enough range of intensity ratios within that same domain to provide precise electron density estimates within instrumental uncertainties. By using atomic data provided by CHIANTI version 7 (Landi et al. 2012), we find that the Fe XII line pair, 186.85/.89 and 192.39 Å, satisfies both of these properties as seen in Figure 4. The intensity ratio range is broad

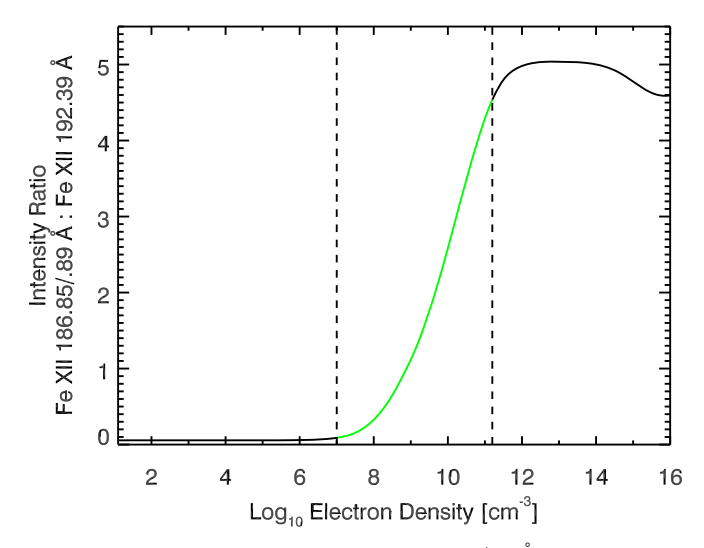


Figure 4. Plot of intensity ratio between Fe XII 186.85/.89 Å and Fe XII 192.39 Å vs. electron density. The dashed lines indicate the lower and upper bounds of the region where a one-to-one relationship between the electron density and the intensity ratio is guaranteed, as indicated by the green section of the plot.

and corresponds to typical quiet-Sun coronal electron density values, spanning from 10⁷ cm⁻³ to about 10¹¹ cm⁻³ where the one-to-one relationship breaks just prior to a local maximum. Physically, Figure 4 shows a transition between two atomic equilibrium states. At low electron densities, the plasma is defined by the absence of collisions where level populations are determined entirely by spontaneous transitions. In contrast, at high electron densities, electron collisions become so overwhelming that collisional de-excitation rivals spontaneous emission, producing a stable state for level populations.

The line pair is also suitable for precise intensity measurements. Examples of the 186.85/.89 and 192.39 Å lines are shown in Figure 5. Here we find a strong, but not uniform, signal throughout the vertical profiles of the lines, approaching spectral radiances on the order of $10^4 \text{ erg}^{-1} \text{ s}^{-1} \text{ cm}^{-2} \text{ sr}^{-1} \text{ Å}^{-1}$. Since the dominant broadening mechanism in the EUV is Doppler broadening, the lines display markedly Gaussian profiles suitable for least-squares fitting. However, the fitting process is only reliable if both lines are unblended with lines from other ion species. This is not a problem for Fe XII 192.39 Å, but the profiles of 186.85/.89 Å do overlap the nearby Ni XI 186.96 Å. However, Ni XI 186.96 Å is over one order of magnitude less intense at its peak than 186.85/.89 Å. Furthermore, their centers are separated enough to allow us to apply a multiple-Gaussian fit (MGF) model. We apply MGFs to each row of both 2 Å wide windows centered on each line of the pair, corresponding to the horizontal ranges seen in Figure 5. Before we apply the fitting routine, we coalign the FOV of the 192.39 Å to that of 186.85/.89 Å by shifting the 192.4 Å window up 0".44 and interpolating accordingly. The MGF model features three parameters applied to each line peak intensity, line width, Doppler shift—and two background parameters—a constant component and a linear component per window. We then determine the integrated intensity of each line using the post-fit peak intensity and line width values, take their ratio, and then apply it to the intensity ratio versus electron density model shown in Figure 4.

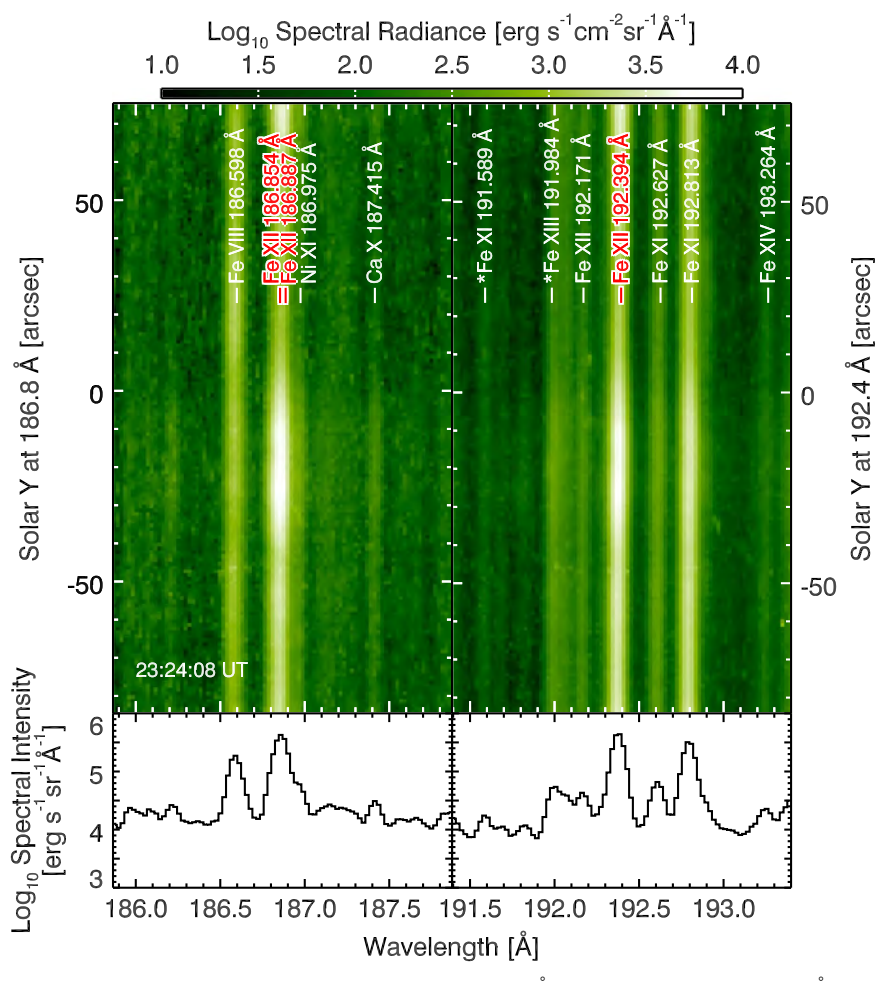


Figure 5. Two spectroscopic windows from the EIS detector centered on Fe XII 186.85/.89 Å (upper left panel) and 192.39 Å (upper right panel) from a full-CCD exposure taken on 2017 August 21 at 23:24:08 UT. These lines are indicated by red labels while nearby lines are labeled in white. Labels preceded by an asterisks (*) indicate theoretical transitions predicted by CHIANTI version 7 (Landi et al. 2012). The lower two panels depict the columnar sums of the spectral radiance, producing plots of the spectral intensity. Note that both windows span slightly different solar Y ranges.

3.2. Temperature Diagnostics via EM Loci Analysis

With electron densities available, we can now apply temperature diagnostics to both the AIR-Spec and EIS data sets. For this, we use EM loci analysis, which we describe similarly to Landi et al. (2002a, 2002b, 2012). First, we express the intensity, Equation (1), in a more useful form:

$$I_{ij}(X^{+m}; \lambda_{ij}) = \frac{1}{4\pi R^2} \int_V G_{ij}(X^{+m}; T, n_e) n_e^2 dV$$
 (4)

where $G(X^{+m}; T, n_e)$ is the contribution function associated with transition $j \rightarrow i$ in ion X^{+m} , defined as

$$G(X^{+m}; T, n_e) \equiv \frac{h\nu_{ij}n_j(X^{+m})A_{ij}(X^{+m})}{n_e^2}$$
 (5)

and T is the plasma temperature of the emission source volume. With electron densities known, the temperature dependence originates solely from $n_j(X^{+m})$ via the total ion species number density, $n(X^{+m})$. The contribution function is useful in this scenario since it allows us to consolidate all the the species-dependent quantities under one value. This becomes important when we assume that the electron density and plasma temperature are uniform and constant values, n_{e0} and T_0 ,

respectively, in the source volume:

$$I_{ij}(X^{+m}; \lambda_{ij}) = \frac{G_{ij}(X^{+m}; T_0, n_{e0})}{4\pi R^2} \int_V n_{e0}^2 dV$$

$$\equiv \frac{G_{ij}(X^{+m}; T_0, n_{e0})}{4\pi R^2} EM$$
(6)

where we define the emission measure, EM $\equiv \int_V n_e^2 dV$, a quantity that does not depend on species-specific properties. We then rearrange Equation (6) as follows:

$$EM = \frac{4\pi R^2 I_{ij}(X^{+m}; \lambda_{ij})}{G_{ij}(X^{+m}; T_0, n_{e0})}.$$
 (7)

Since the emission measure is the same regardless of ion species or transition, the right-hand side of Equation (7) must be as well. This leads us to define the following function:

$$EML(T) \equiv \frac{I_{ij}(X^{+m}; \lambda_{ij})}{G_{ij}(X^{+m}; T, n_{e0})}$$
(8)

which we name the EM loci. From here, we can establish the diagnostic: if the temperature and electron density are uniform and constant within a given source volume, then there exists a characteristic isothermal temperature value for that volume, T_0 ,

such that $\mathrm{EML}(T_0)$ is the same for all transitions and all ion species. In practice, this means we can use the measured values of n_{e0} from the process outlined in Section 3.1 to calculate contribution functions within a broad temperature range and then, using our measured values of I_{ij} , we can determine the EM loci for each emission line detected in the EIS and AIR-Spec data sets. We can then check if all the EM loci curves intersect at a common temperature value. If so, then the plasma in the source volume can be approximated as isothermal with characteristic temperature T_0 . For the purposes of this work, we establish a modified definition of the EM loci we denote as EML^* which holds the same diagnostic properties as EML but instead consolidates all observed lines of a single ion species:

$$EML^{*}(T) \equiv \sum_{ij \in X^{+m}} I_{ij}(X^{+m}; \lambda_{ij}) / \sum_{ij \in X^{+m}} G_{ij}(X^{+m}; T, n_{e0}) \quad (9)$$

which allows for greater effective signal for each instance of the EM loci function. We calculate contribution functions in terms of temperature for each transition using the electron density values measured in Section 3.1 and solving for $n_j(X^{+m})$ in Equation (2) using a model of solar elemental abundances (Asplund et al. 2009), and a model of ionization equilibrium and other atomic values from CHIANTI version 7.

It is important to take a moment to discuss what exactly we mean by *isothermal temperature* in this context. Our electron density and temperature diagnostics operate under the assumption that the temperature of plasma in a volume bounded by the line of sight is constant on timescales comparable to the exposure time of a single EIS raster step. This informs our definition of *isothermal* as being a local descriptor instead of global one. In other words, we are saying that only the plasma contained in the line of sight of a single spatial pixel defined by the EIS raster may be approximated as an isothermal plasma with a characteristic temperature. Under this definition, the temperature is allowed to vary from pixel to pixel. We do not imply that the entire volume of plasma in the EIS FOV is globally isothermal. To avoid confusion, we use the term *line-of-sight isothermal* to denote when our local definition applies.

We apply EM loci analysis to both the EIS and AIR-Spec data sets. The EIS data set provides a robust measurement of the line-of-sight isothermal temperatures which we can use to verify the effectiveness of the analysis as applied to the AIR-Spec IR spectra. We begin analysis on the EIS data by identifying as many suitable emission lines as possible in the full-CCD readout. We only select lines that satisfy the following properties: (1) the lines must be detected up to 5σ at all raster positions, and (2) the lines must be free of all unresolved blends with lines from other ion species. Twentyseven lines satisfy these properties, representing seven distinct ion species: Si X, S X, and Fe X-XIV. All lines and their associated transitions are listed in Table 3. We first coalign the vertical axis at the central wavelength of each emission line to the 186.8 Å FOV, accounting for the wavelength-dependent vertical drift of the EIS detector readout. We then calculate the EML* function for each of these seven ion species and search for an intersection point common to all of them, doing so for spectra sampled at each detector row and raster step. The search algorithm we use to find these intersections operates by pairing every possible combination of EML* curves and calculating secant lines for both curves in every pair. A single secant is anchored by two points on its associated EML* function, each

Table 3
EIS EUV Lines Used for EM Loci Temperature Analysis

		*	•
Ion	Wavelength (Å)	Lower State	Upper State
Si X	253.790	$2s^22p^{-2}P_{1/2}$	$2s2p^2 {}^2P_{3/2}$
	258.374	$2s^22p^2P_{3/2}$	$2s2p^2 {}^2P_{3/2}$
	261.056	$2s^22p^2P_{3/2}$	$2s2p^2 {}^2P_{1/2}$
	271.992	$2s^22p^2S_{1/2}$	$2s2p^2 {}^2S_{1/2}$
	277.264	$2s^22p^2P_{3/2}$	$2s2p^2 {}^2S_{1/2}$
S X	259.497	$2s^22p^3 ^4S_{3/2}$	$2s2p^4 ^4P_{3/2}$
	264.231	$2s^22p^3 ^4S_{3/2}$	$2s2p^4 ^4P_{5/2}$
Fe X	174.531	$3s^23p^5 {}^2P_{3/2}$	$3s^23p^43d^{-2}D_{5/2}$
	177.240	$3s^23p^5 {}^2P_{3/2}$	$3s^23p^43d^{-2}P_{3/2}$
	184.537	$3s^23p^5 {}^2P_{3/2}$	$3s^23p^43d^{-2}S_{1/2}$
	207.449	$3s^23p^5 {}^2P_{3/2}$	$3s^23p^43d^2F_{5/2}$
Fe XI	180.401	$3s^23p^4 {}^2P_2$	$3s^23p^33d^{-3}D_3$
	182.167	$3s^23p^4 \ ^3P_1$	$3s^23p^33d^{-3}D_2$
	188.216	$3s^23p^4 \ ^3P_2$	$3s^23p^33d^{-3}P_2$
	192.813	$3s^23p^4 \ ^3P_1$	$3s^23p^33d^{-3}P_2$
	202.424	$3s^23p^4 \ ^3P_2$	$3s^23p^33d^{-3}P_2$
Fe XII	186.854	$3s^23p^3 {}^2D_{3/2}$	$3s^23p^23d^2F_{5/2}$
	186.887	$3s^23p^3 {}^2D_{5/2}$	$3s^23p^23d^2F_{7/2}$
	192.394	$3s^23p^3 ^4S_{3/2}$	$3s^23p^23d^4P_{1/2}$
	193.509	$3s^23p^3 ^4S_{3/2}$	$3s^23p^23d^4P_{3/2}$
	195.119	$3s^23p^3 ^4S_{3/2}$	$3s^23p^23d^4P_{5/2}$
Fe XIII	200.021	$3s^23p^2 \ ^3P_1$	$3s^23p3d\ ^3D_2$
	202.044	$3s^23p^2 ^3P_0$	$3s^23p3d^{-3}P_1$
	251.952	$3s^23p^2 \ ^3P_2$	$3s3p^3 \ ^3S_1$
Fe XIV	211.317	$3s^23p^2P_{1/2}$	$3s^23d^{-2}D_{3/2}$
	264.789	$3s^23p^2P_{3/2}$	$3s3p^2 {}^2P_{3/2}$
	270.521	$3s^23p^{-2}P_{3/2}$	$3s3p^2 {}^2P_{1/2}$
	270.521	/	

of which is evaluated at temperatures separated by $\Delta \log_{10} T[\mathrm{K}] = 0.003$. The EML* pair is considered to be intersecting if the secants intersect in a temperature range bounded by the anchor points. In these instances, the recorded temperature would be that associated with the secant intersection point.

With a complete catalog of intersections for each set of EML* curves at each detector row and raster position, we now determine whether a genuine common intersection exists for each of those sets. However, this is not a trivial task since any given pair of EML* curves can intersect each other multiple times. This results in several isolated intersection points at extreme temperatures that are meaningless in the context of the temperature diagnostic. To distinguish the points contributing to a common intersection from those that are incidental and isolated, we apply a clustering algorithm to each EML* set. First, each coordinate axis is transformed from a logarithmic to a linear scale and then normalized to range from 0 to 1, corresponding to the minimum and maximum values, respectively, of T and EML*(T). The algorithm then focuses on the leftmost intersection point which we call the target point. The normalized distances from the target point to every other point are then calculated. Next, we fill the coordinate space with concentric rings of equal width centered on the target point. The ring width is initially set to the equivalent normalized length of T = 200 K on the x-axis. If at least seven other intersection points lie within the central ring under the initial conditions, then the target point is automatically considered to be part of a cluster and no further testing is required. If not,

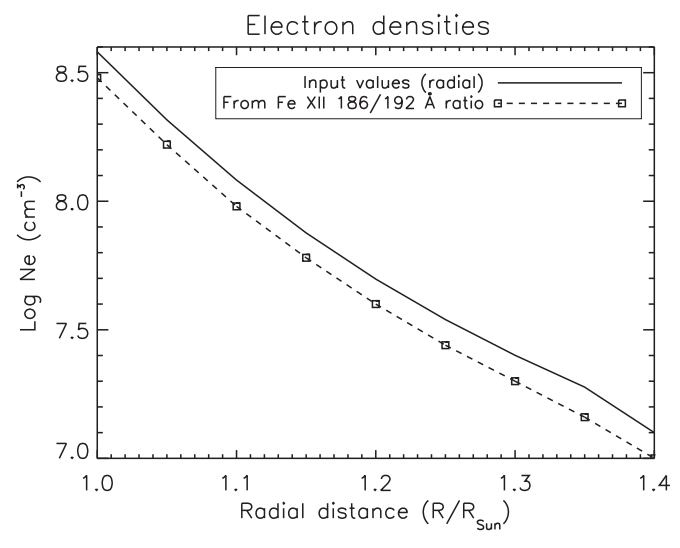


Figure 6. Radial semi-empirical model of electron density in a quiet-Sun streamer based on *SoHO* Ultraviolet Coronagraph Spectrometer observations of coronal lines out to 3.1 solar radii (solid line), and the predicted electron densities from ratios of EIS Fe XII intensities derived from the semi-empirical model (squares and dashed line).

then we gradually increase the ring width by increments of 200 K until one of the two following conditions are met: (1) the ring size exceeds 200,000 K, or (2) at least seven points lie within one ring. If condition (1) occurs then the target point is deemed not to be part of a cluster. If condition (2) occurs, then we check that the points lie within the central ring. If not, then we consider the target point to be not part of a cluster; if so, then we consider the target point to be part of a cluster. We then repeat this process for all intersection points. Next, we check for multiple clusters by ensuring that no two intersection points identified as clustered are farther than 300,000 K apart. This leaves us with the following three ending scenarios: (1) there is a single cluster of intersection points, (2) there are multiple clusters of intersection points, or (3) there are no clusters of intersection points. For scenario (1), we consider the characteristic isothermal temperature of the plasma along the line of sight to be the mean temperature of the cluster points. For scenarios (2) and (3), we consider the EM loci method to have failed and do not record a temperature for that location.

The AIR-Spec data require a modified approach. Unlike the EIS data, the AIR-Spec data do not benefit from having a large number of detected lines. Each of the four lines corresponds to a unique ion species, so we do not use the modified EM loci function, EML*, applied to the EIS data. Instead, we slightly modify Equation (8) by replacing the contribution function, G_{ij} , with the volume emissivity, ϵ_{ij} . This allows us to incorporate radiative processes that may influence the IR lines but not the far more resilient EUV lines. In particular, the IR lines are strongly affected by photoexcitation. To obtain an EM loci plot equivalent to the usual one for the EUV lines, we need to assume a model for the plasma distribution. For simplicity, we assumed a homogeneous distribution of the electron density with cylindrical symmetry and the radial variation plotted in Figure 6. To calculate the contribution of photoexcitation, we used the combined quiet-Sun irradiance data described in Woods et al. (2009), which used a continuum up to $2.4 \mu m$ observed by the Spectral Irradiance Monitor (Harder et al. 2005) onboard the Solar Radiation and Climate Experiment (SORCE). Above 2.4 μ m, we used a blackbody with a

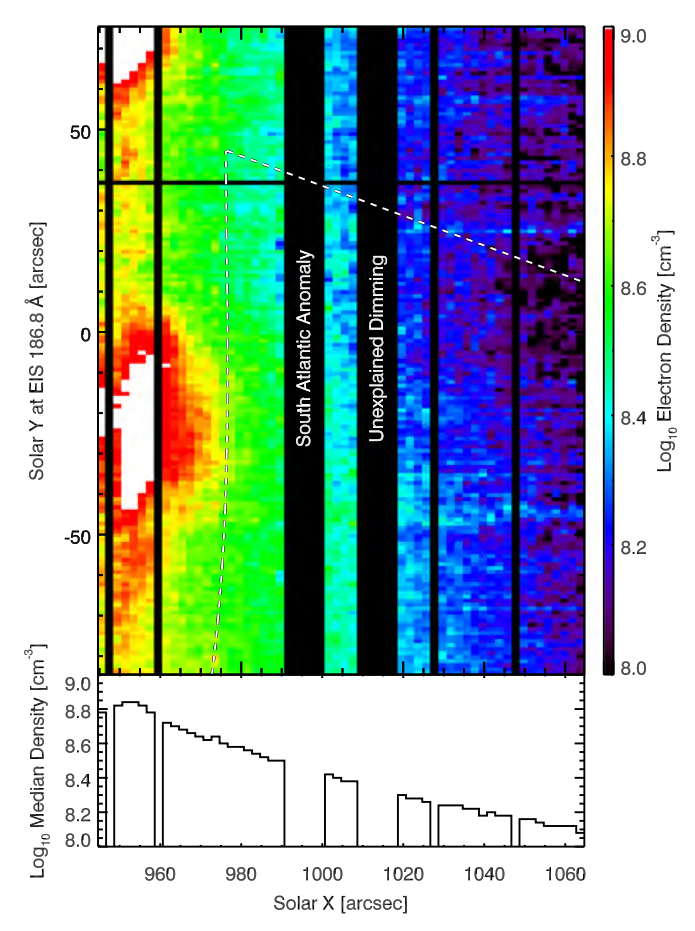


Figure 7. Map of line-of-sight-integrated electron densities throughout the EIS field of view (top panel). Black vertical and horizontal bars indicate data not included in the analysis due to the South Atlantic anomaly, the unexplained dimming event, frame dropouts, or other detector defects. The dashed line indicates the northeastern boundary of the AIR-Spec field of view. The lower panel depicts the columnar median of electron density values across the solar *X* dimension of the EIS field of view. Bootstrapped standard errors of the median values are too small to meaningfully represent on the plot.

temperature of 6100 K. To complete the calculation, we converted irradiances to disk radiances assuming uniform disk brightness. Finally, the AIR-Spec data do not benefit from the strong signal-to-noise ratio that the EIS data have. So, instead of applying the EM loci analysis to each detector row and raster position, we instead coadded the spectra across all exposures throughout two annular regions 31" wide, centered at two radial distances from the solar limb: 30" and 100".

4. Results and Discussion

4.1. Electron Densities

As seen in Figure 7, the strong signal-to-noise ratio of Fe XII 186.85/.89 Å and Fe XII 192.39 Å throughout the observation allowed us to produce a detailed map of the coronal electron density resolved to instrumental limits. This map depicts vertically averaged electron densities spanning from $10^{8.08\pm0.01}$ cm $^{-3}$ at the western extreme of the EIS FOV to $10^{8.92\pm0.02}$ cm $^{-3}$ along the solar limb.

We find a strong correlation between the electron density structure of the coronal plasma and the morphological features depicted in the AIA images of the same region seen in Figure 3. Two localized elliptical regions containing the highest densities just off the limb—one spanning from Y = -50'' to 0'', and the

other spanning from Y = 50'' to some location north of the FOV—are cospatial with intensity enhancements seen in AIA 193 and 211 Å, which overlap the wavelength range of EIS, and to a lesser extent 94 and 335 Å. The enhancements appear to be the setting remnants of small-scale flux emergence unassociated with an active region. Although they are near the likely footpoints of the prominence, the enhancements are unlikely to be related since the prominence does not appear to undergo any activation or eruption during or after the EIS observations. Additionally, at the far western end of the map centered near Y = 0'' is a semi-circular region of excess density depletion. This is cospatial with the eastern end of a large coronal cavity seen in AIA 193 Å which formed coincident to the prominence.

The electron density decays remarkably smoothly from the limb outward and is not affected by the prominence as the latter mostly emits at lower temperatures. The bottom panel of Figure 7 shows the median electron density in each column of the map. With the exception of the small sliver east of X = 950occupied by the solar disk, and despite the South Atlantic anomaly, unexplained dimming phenomenon, and numerous frame dropouts, this plot shows a clear exponential decay of electron density consistent with other quiet-Sun measurements. For example, the solid line of Figure 6 shows a radial semiempirical model of the electron density in a quiet-Sun streamer obtained by Del Zanna et al. (2018) from the SoHO Ultraviolet Coronagraph Spectrometer (UVCS; Kohl et al. 1995) observations of coronal lines out to 3.1 solar radii. We have taken this semi-empirical radial model and calculated, assuming spherical symmetry, the predicted radiances in the EIS Fe XII lines integrated along the line of sight using CHIANTI atomic data. We have then considered these radiances as real observations and obtained from their ratio a predicted density averaged along the line of sight using the same atomic data. These results are plotted in the same figure and show that the predicted electron densities, between 10^{8.1} and 10^{8.2} cm⁻³, agree quite well with the observed values.

4.2. Line-of-sight Isothermal Temperatures and IR Diagnostic Potential

The EM loci temperature diagnostics were successful across the vast majority of the EIS data set. All sampled locations in the FOV produced a clustered set of intersection points with the exception of two detector rows at the bottom of the FOV where there were insufficient data from long-wavelength windows due to the wavelength-dependent vertical shift of the EIS spectra. Figure 8 depicts a typical EM loci plot for a single sample within the EIS data set. It demonstrates a tightly bound cluster of intersection points within a temperature range of $10^{6.1}$ – $10^{6.2}$ K, a feature we found to be ubiquitous across all but a few samples. As a result, we can produce a similarly wellresolved map of the isothermal temperature, seen in Figure 9, as we did for the electron density analysis. The map shows vertically averaged temperatures spanning from $10^{6.12} \pm 10^{3.5}$ K along the limb to $10^{6.19} \pm 10^{3.5}$ K along the western edge of the EIS FOV. As is the case with the electron density map, the isothermal temperature exhibits a smooth, exponential trend as seen in the bottom panel of Figure 9; however, unlike the electron density, the isothermal temperature generally increases with distance from limb as expected for quiescent lower coronal plasma. It should be noted that the temperature only varies by about 300,000 K across the entire AIR-Spec FOV, so

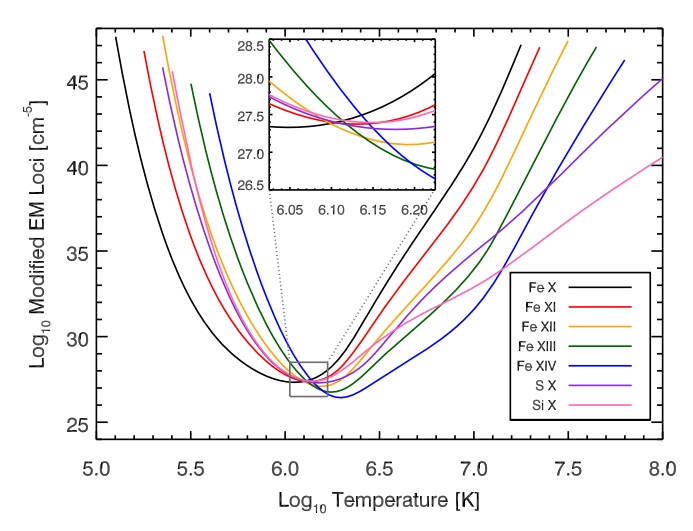


Figure 8. Example of modified EM loci (EML*) functions calculated for seven ions associated with emission lines detected by EIS. This example was constructed from data sampled near solar (X,Y)=(966,11) arcsec. The EML* curves show a strong tendency to intersect one another near $T=10^{6.1}$ K, indicating an approximately isothermal volume of plasma along the line of sight characterized by that temperature. The inset plot in the top center provides a magnified view of the intersection region bounded by the dark gray box. Note that uncertainties are too small to meaningfully depict on the plot.

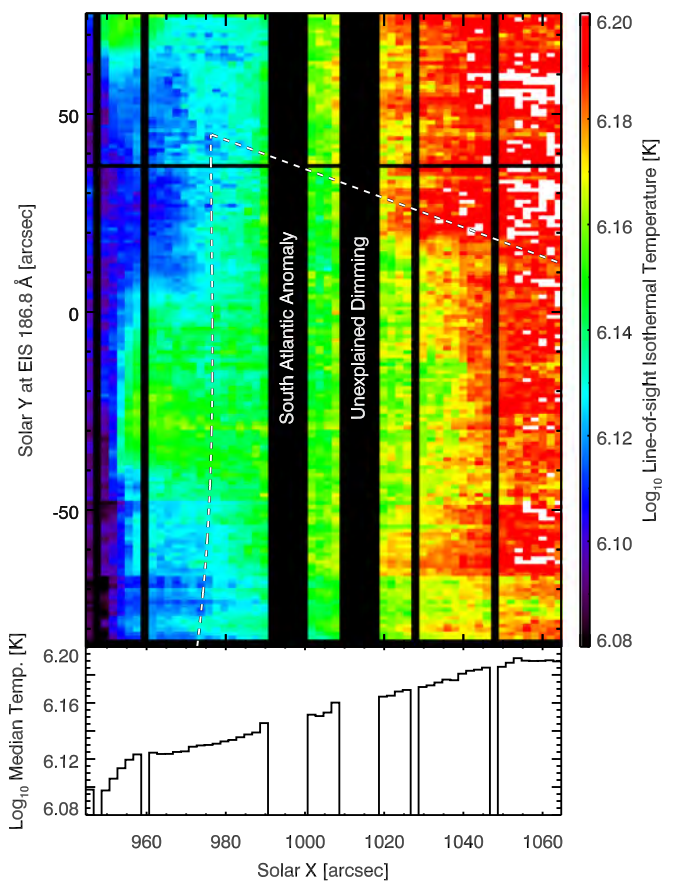


Figure 9. Map of line-of-sight isothermal temperatures derived from EM loci analysis in the EIS field of view (top panel). Black vertical and horizontal bars indicate data not included in the analysis due to the South Atlantic anomaly, the unexplained dimming event, frame dropouts, other detector defects, or failure of the EML* curves to form a precise intersection point. The dashed line indicates the northeastern boundary of the AIR-Spec field of view. The lower panel depicts the columnar median of temperature values across the solar *X* dimension of the EIS field of view. Bootstrapped standard errors of the median values are too small to meaningfully represent on the plot.

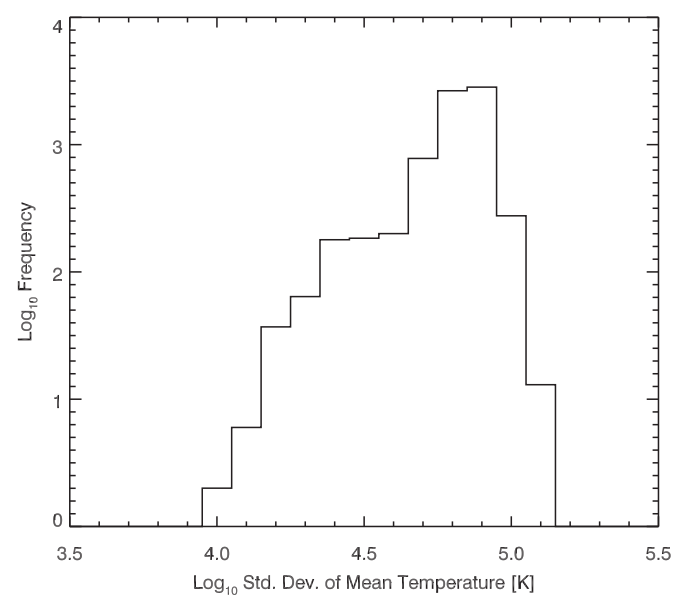


Figure 10. Histogram of uncertainties (i.e., standard deviations of the mean) for temperatures sampled throughout the EIS field of view by applying EM loci analysis to the EIS spectral data.

we must pay close attention to the uncertainties arising from the EM loci method. Figure 10 shows a histogram of the standard deviations of the mean temperature sampled throughout the AIR-Spec FOV using the EM loci method. We use this value as an indication of the spread inherent in the EM loci intersection points, providing a meaningful indicator of uncertainty. We find a vast majority of these values in the range of $10^{4.5}$ – $10^{4.9}$ K, with no uncertainties beyond $10^{5.1}$ K, well below 300,000 K variation in mean temperatures and also below the 200,000 K upper limit for cluster width.

We also see a correlation between the localized intensity enhancements seen in AIA 94, 193, 211, and 335 Å-four passbands which tend to image hotter plasma than the otherstemperature enhancements on the order $\Delta \log_{10} T[\vec{K}] = 0.04$. It is unclear whether the prominence influenced the temperature diagnostics. Other than the temperature enhancements near the limb, the only anomalous temperature deviation appears in a region bounded by solar $X = 1020 \rightarrow 1040 \text{ arcsec}$ and solar $Y = -50 \rightarrow 20 \text{ arcsec}$. This region is characterized by an intrusion of cooler plasma on the order of $10^{6.16}~\rm K$ into the $10^{6.20}~\rm K$ plasma near the western edge of the FOV. This is cospatial with the farthest reaches of the main prominence arch; however, since there is no apparent signature of the prominence in the electron density structure, it is unclear whether it is related to this temperature feature. Furthermore, the region is bounded from below by what appears to be a horizontal discontinuity. This is an artefact arising from a peculiarity in the EIS spectra: the increasingly northward shift of the slit FOV with increasing wavelength. It represents the southern extent of the FOV for the first longwavelength passband of the full-CCD readout. South of this point, the number of available species for EM loci analysis drops, which appears to have some systematic effect of the temperature measurements. Given this, it is difficult to say whether the lower-temperature structure is correlated with the contour of the prominence arch or simply a continuation of a larger lower-temperature structure originating from below the FOV. Overall, the results of the EM loci analysis on the EIS

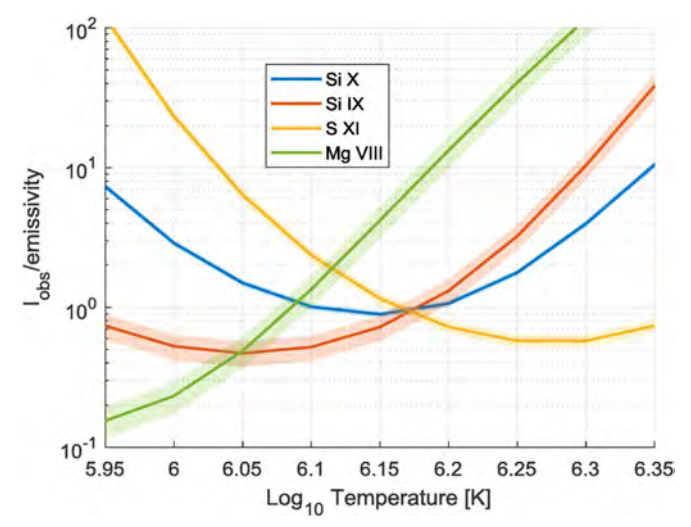


Figure 11. Plot of observed AIR-Spec IR line intensities sampled across a radial range of $31^{\prime\prime}$ centered at $30^{\prime\prime}$ from the solar limb divided by the volume emissivity, which we use as a proxy for the EM loci function. The shaded envelopes around the curves depict the 95% confidence interval due to uncertainties arising from Gaussian fits to the line profiles. The intersection points are more spread out than those seen in the EIS data, but are still compact enough to show line-of-sight isothermal temperatures in the range of $10^{6.0}-10^{6.2}$ K.

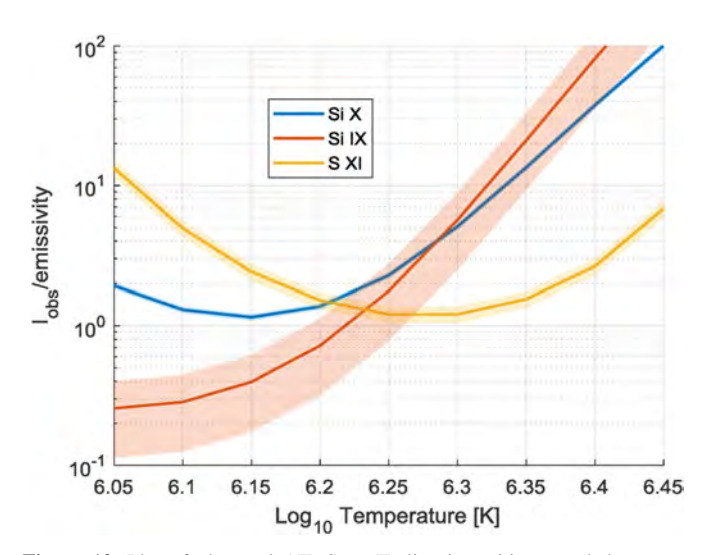


Figure 12. Plot of observed AIR-Spec IR line intensities sampled across a radial range of 31" centered at 100" from the solar limb divided by the volume emissivity, which we use as a proxy for the EM loci function. The shaded envelopes around the curves depict the 95% confidence interval due to uncertainties arising from Gaussian fits to the line profiles. The weakest line, Mg VIII 3.03 μ m, was not detected at this location. Although the number of intersection points is small, there is a noticeable shift toward higher temperatures than depicted in Figure 11.

data appear reliable and can serve as a good benchmark for the AIR-Spec temperature measurements.

The EM loci analysis of the AIR-Spec data, although not as robust, is consistent with the EIS results. Figures 11 and 12 depict the results of the EM loci analysis for AIR-Spec data centered at 30" and 100" from the solar limb, respectively, both of which sample spectra across a radial range of 31". The shaded bands indicate 95% confidence intervals due to uncertainty in the Gaussian fits to each line. Errors in the AIR-Spec radiometric calibration and modeled volume emissivity are not indicated, but likely contribute to the spread in intersection points of the EM loci curves.

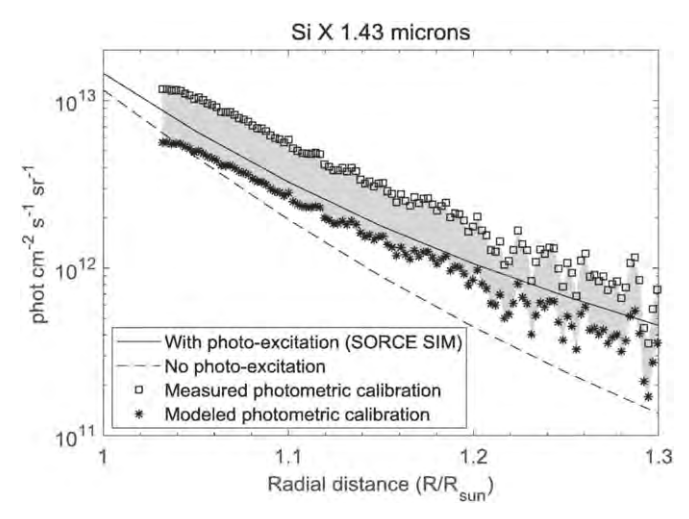


Figure 13. Predicted radial decrease of the strongest AIR-Spec line, Si \times 1.43 μ m, with photoexcitation from the *SORCE* Total Irradiance Monitor (solid line) and without photoexcitation (dashed line). The observed radiances are shown for two different photometric calibrations of AIR-Spec, measured (boxes) and modeled (asterisks).

Both samples display a spread of intersection points broader than what is typically seen in the EIS data, and neither sample would pass the strict clustering standards established for the EIS data in Section 3.2. However, this does not wholly invalidate the results of the AIR-Spec temperature diagnostics, since both show central tendencies consistent with EIS temperature measurements. For the 30" sample, the 10 EM loci intersections span a range of temperatures from 10^{6.05} to $10^{6.17}$ K with a variance-weighted mean temperature of $10^{6.13 \pm 0.02}$ K. Note that the variances for the intersection points derive entirely from the Gaussian fits to the AIR-Spec lines. For the 100" sample, we only have three intersections since Mg VIII 3.03 μ m was not detected at this distance from the limb. The intersections span a range of warmer temperatures from $10^{6.20}$ to $10^{6.28}$ K with a variance-weighted mean temperature of $10^{6.21\pm0.01}$ K. Both mean temperatures are consistent with their EIS counterparts, capturing the overall outwardly increasing trend of the quiescent coronal plasma temperature. Note that the reported uncertainties are dispersioncorrected standard deviations of the variance-weighted means. When scaled logarithmically, the uncertainty spits into unequal upper and lower components; however, since these components do not differ by more that 0.01 in both cases, we simply quote a single uncertainty down to that precision.

We must address the breakdown of physical assumptions that are valid in the EUV but not in the IR. Of critical interest is the effect of photoexcitation from the solar IR continuum. We attempted to correct for this by using the volume emissivity, ϵ_{ij} , in place of the contribution function, G_{ij} , for the IR EM loci analysis. This allowed us to account for photoexcited effects on level populations. Figure 13 shows the radial change in radiance for the Si \times 1.43 μm observed by AIR-Spec and two predictions of the same value derived from CHIANTI. One prediction accounts for photoexcitation using continuum irradiance measurements from the Total Irradiance Monitor (Kopp & Lawrence 2005) onboard SORCE while the other does not. The observed radiances were calibrated using two different methods, described in Section 2.1. The line radiance is about two times greater when the calibration is based on photospheric measurements rather than estimates of the

geometric area and optical efficiencies, giving an indication of the uncertainty in both methods. The photoexcited model predicts radiances that lie between the two calibrations. The radial decay of AIR-Spec Si X 1.43 μm radiances agrees strongly with the photoexcited model within the EIS FOV (i.e., within 1.1 R_{\odot}). Although the agreement is promising, it does not rule out dramatic systematic changes of the near-limb AIR-Spec Si X 1.43 μm radiances due to local continuum enhancements or variations due to the solar cycle.

The cool plasma from the prominence also introduces uncertainty into the analysis. The plasma trapped in the prominence likely originates from the upper chromosphere where we typically find partially ionized plasma at temperatures approaching 10° K. It is unlikely that the prominence will achieve ionization equilibrium with the ambient coronal plasma on our observational timescales, meaning it cannot act as a strong source of coronal emission lines from ion species typically observed in the EUV, such as Si IX, Si X, and S XI. Similarly, it is also unlikely that the prominence is a strong source of additional IR continuum not accounted for in our photoexcitation calculations. However, there is a likelihood of cooler transition region emission lines, such as those originating from Mg VIII, forming at the interface of the cool prominence core and ambient coronal plasma. Figure 11 features Mg VIII 3.03 μ m, a line that forms at cooler temperatures than the other AIR-Spec lines and is only seen near the limb. The EM loci curve associated with this line strays far from the common intersection point of the other three EM loci functions ($\sim 10^{6.17}$ K), trending toward cooler temperatures. It is possible that the this is an indication of a two-component plasma, a quiet-Sun component that occupies the entire AIR-Spec FOV and a cooler prominence component only observed near the limb. However, there is considerable uncertainty surrounding this claim as we only provide one instance of this phenomenon and more EM loci curves associated with cooler lines are needed to distinguish between two distinct intersection points and a single intersection point encumbered by additional sources of uncertainty.

Finally, it is important to address the role atomic abundances play in the EM loci analysis. Precise intersections will only form under isothermal conditions in the line-of-sight source volume if we assume the correct abundances for all atomic species involved. In this work, we assume photospheric abundances from Asplund et al. (2009), which we find approximate the coronal abundances well for the four atomic species that take part in the analysis: Mg, Si, S, and Fe. Del Zanna et al. (2018) found abundances for Mg and Si in the near-limb, quiet-Sun corona close to their respective photospheric values after reprocessing SUMER and UVCS data. This is consistent with the observed first ionization potential (FIP) bias for coronal abundances where elements with high FIP, such as O (13.6 eV), are far more underrepresented in the corona when compared to their photospheric values than elements of relatively low FIP, such as Mg (7.6 eV) and Si (8.2 eV) (e.g., Raymond et al. 1997). According to this effect, we also expect Fe (7.9 eV) to be near photospheric abundance in the corona, with the possibility of a slight enhancement (e.g., Aschwanden et al. 2003; Phillips 2012). However, it is unclear how the FIP bias affects the coronal abundance of an element with intermediate FIP, such as S (10.4 eV). In this case, the results of our EM loci analysis as applied to the EIS and AIR-Spec lines indicate that the coronal abundance of S is also close

to the Asplund et al. (2009) photospheric value. This is in agreement with a recent re-analysis of a *SoHO* SUMER offlimb observation of the quiet Sun by Del Zanna & DeLuca (2018), where the relative abundances of low-, mid-, and high-FIP elements were found to be close to the Asplund et al. (2009) photospheric values.

5. Conclusions

In this work, we used coordinated EUV and IR spectral observations of the 2017 August 21 total solar eclipse to characterize coronal plasma near the limb. Full-CCD EIS observations provided robust diagnostics for electron densities. This made EM loci temperature diagnostics possible for both the EIS and AIR-Spec data sets. We found consistent temperature measurements for both data sets, featuring an outward increase from about about 10^{6.1} K near the limb to about 10^{6.2} K around 100" from the limb. We conclude that IR emission lines have great potential to act as temperature diagnostics for coronal plasma when coupled with electron density measurements from coordinated EUV spectral observations.

However, this conclusion is not without some uncertainty, especially considering the difference in quality between the EIS and AIR-Spec data sets. We expect to remedy this during the second flight of AIR-Spec on 2019 July 2 to observe a total solar eclipse over the southern Pacific Ocean. The 2019 observation will feature increased sensitivity and reduced jitter. Improvements to thermal shielding in the IR camera and spectrometer will reduce the background level by a factor of 15–25, improving the signal-to-noise ratio by a factor of 4–5. Closing the loop on the image stabilization system will reduce the jitter by a factor of 20, allowing us to better coordinate with other observatories by targeting precise locations in the corona or scanning the slit systematically.

Our results bear considerable importance with regards to anticipated advancements in ground-based IR observations of the Sun. Of particular interest is DKIST, which is under construction at the Haleakala Observatory in Hawaii, USA. This observatory will boast a state-of-the-art suite of visible and IR instruments, including the Cryogenic Near-infrared Spectropolarimeter (Fehlmann et al. 2016) and the Diffraction-limited Near-infrared Spectro-polarimeter (Elmore et al. 2014), capable of observing at least three of the four AIR-Spec target lines (Si X 1.431 μ m, Mg VIII 3.03 μ m, and Si IX 3.94 μ m) as well as other IR coronal lines with potential diagnostic significance (e.g., Fe XIII 1.07 μ m, Fe IX 2.22 μ m, and Si IX 2.58 μ m.) Unlike AIR-Spec, DKIST will observe the outer corona daily over a much larger collecting area. However, DKIST will be limited to observing one spectral line at a time and, being a ground-based observatory, will not have access to as many physical diagnostics as AIR-Spec. Regardless, the near-IR data gathered by AIR-Spec will be important for planning DKIST observations. Finally, coordinated EUV spectral observations will prove to be invaluable in both evaluating the diagnostic value of DKIST's observed IR lines and providing critical supplementary information needed for a complete physical characterization of coronal plasma.

The authors would like to thank the anonymous referee for their exceptional feedback which greatly improved the quality of this work. *Hinode* is a Japanese mission developed and launched by ISAS/JAXA, collaborating with NAOJ as a

domestic partner, and NASA and UKSA as international partners. Scientific operation of the *Hinode* mission is conducted by the *Hinode* science team organized at ISAS/JAXA. This team mainly consists of scientists from institutes in the partner countries. Support for the post-launch operation is provided by JAXA and NAOJ (Japan), UKSA (UK), NASA, ESA, and NSC (Norway). EUV context imaging is courtesy of NASA/*SDO* and the AIA science team. AIR-Spec was developed under an NSF Major Research Instrumentation grant, AGS-MRI 1531549, with cost sharing by The Smithsonian Institution. G.DZ. acknowledges support by STFC (UK) via the consolidated grant of the DAMTP atomic astrophysics group (ST/P000665/1) at the University of Cambridge.

ORCID iDs

Chad A. Madsen https://orcid.org/0000-0001-8775-913X Jenna E. Samra https://orcid.org/0000-0002-4498-8706 Giulio Del Zanna https://orcid.org/0000-0002-4125-0204 Edward E. DeLuca https://orcid.org/0000-0001-7416-2895

References

```
Anzer, U., Heinzel, P., & Fárnik, F. 2007, SoPh, 242, 43
Aschwanden, M. J., Schrijver, C. J., Winebarger, A. R., & Warren, H. P. 2003,
Asplund, M., Grevesse, N., Sauval, A. J., & Scott, P. 2009, ARA&A, 47, 481
Bao, X., Zhang, Z., Deng, J., et al. 2009, ScChG, 52, 1794
Blackwell, D. E. 1952, MNRAS, 112, 652
Byard, P. L., & Kissell, K. E. 1971, SoPh, 21, 351
Culhane, J. L., Harra, L. K., James, A. M., et al. 2007, SoPh, 243, 19
Del Zanna, G., & DeLuca, E. E. 2018, ApJ, 852, 52
Del Zanna, G., & Mason, H. E. 2018, LRSP, 15, 5
Del Zanna, G., Raymond, J., Andretta, V., Telloni, D., & Golub, L. 2018, ApJ,
   865, 132
Dima, G. I., Kuhn, J. R., Mickey, D., & Downs, C. 2018, ApJ, 852, 23
Doschek, G. A., & Feldman, U. 1977, A&A, 58, L13
Dwivedi, B., Mohan, A., & Thomas, R. 1998, SoPh, 180, 157
Dwivedi, B. N., & Gupta, A. K. 1993, SoPh, 146, 397
Dzifčáková, E., & Kulinová, A. 2010, SoPh, 263, 25
Eddy, J. A., & McKim Malville, J. 1967, ApJ, 150, 289
Einstein, A. 1916, DPhyG, 18, 318
Elmore, D. F., Rimmele, T., Casini, R., et al. 2014, Proc. SPIE, 9147, 914707
Fehlmann, A., Giebink, C., Kuhn, J. R., et al. 2016, Proc. SPIE, 9908, 99084D
Feldman, U. 1981, PhyS, 24, 681
Feldman, U., Doschek, G. A., & Cohen, L. 1983, ApJ, 273, 822
Firor, J., & Zirin, H. 1962, ApJ, 135, 122
Harder, J., Lawrence, G., Fontenla, J., Rottman, G., & Woods, T. 2005, SoPh,
Harrison, R. A., Sawyer, E. C., Carter, M. K., et al. 1995, SoPh, 162, 233
Hodapp, K.-W., MacQueen, R. M., & Hall, D. N. B. 1992, Natur, 335, 707
Judge, P. G. 1998, ApJ, 500, 1009
Kastner, S. O. 1993, SoPh, 143, 197
Kayshap, P., Banerjee, D., & Srivastava, A. K. 2015, SoPh, 290, 2889
Keil, S. L., Rimmele, T. R., & Wagner, J. 2009, EM&P, 104, 77
Kohl, J. L., Esser, R., Gardner, L. D., et al. 1995, SoPh, 162, 313
Kopp, G., & Lawrence, G. 2005, SoPh, 230, 91
Kurt, V. G. 1962, SvA, 6, 349
Lamy, P., Kuhn, J. R., Lin, H., Koutchmy, S., & Smartt, R. N. 1992, Sci,
   257, 1377
Landi, E., Del Zanna, G., Young, P. R., Dere, K. P., & Mason, H. E. 2012,
Landi, E., Feldman, U., & Dere, K. P. 2002a, ApJ, 574, 495
Landi, E., Feldman, U., & Dere, K. P. 2002b, ApJ, 139, 281
Lang, J., Kent, B. J., Paustian, W., et al. 2006, ApOpt, 45, 8689
Lemen, J. R., Title, A. M., Akin, D. J., et al. 2012, SoPh, 275, 17
Mackovjak, Š., Dzifčáková, E., & Dudík, J. 2013, SoPh, 282, 263
McIntosh, S. W., de Pontieu, B., & Leamon, R. J. 2010, SoPh, 265, 5
Mizutani, K., Maihara, T., Hiromoto, N., & Takami, H. 1984, Natur, 312, 134
Monsignori Fossi, B. C., & Landini, M. 1994, A&A, 284, 900
Neupert, W. M., Epstein, G. L., Thomas, R. J., & Thompson, W. T. 1992,
   SoPh, 137, 87
```

```
Olsen, K. H., Anderson, C. R., & Stewart, J. N. 1971, SoPh, 21, 360
Pasachoff, J. M., & Muzyka, D. F. 1976, VA, 19, 341
Pasachoff, J. M., Sanford, M. T., II, & Keller, C. F., Jr. 1978, BAAS, 10, 431
Phillips, K. J. H. 2012, MNRAS, 421, 1757
Pike, C. D., & Harrison, R. A. 2000, A&A, 362, L21
Pottasch, S. R. 1963, ApJ, 137, 945
Raymond, J. C., Kohl, J. L., Noci, G., et al. 1997, SoPh, 175, 645
Reeves, E. M., Noyes, R. W., & Withbroe, G. L. 1972, SoPh, 27, 251
Samra, J., Cheimets, P., DeLuca, E., et al. 2016, Proc. SPIE, 9908, 99085U
Samra, J. E., Judge, P. G., DeLuca, E. E., & Hannigan, J. W. 2019, ApJL, 873, 25
Shimizu, E., Ali, S., Tsuda, T., et al. 2017, A&A, 601, A111
```

Singh, J., Sakurai, T., Ichimoto, K., & Takeda, A. 2002, PASJ, 54, 807

```
Tayal, S. S., & Henry, R. J. W. 1988, ApJ, 329, 1023
Taylor, J. H., & MacQueen, R. M. 1964, ApOpt, 3, 1365
Tollestrup, E. V., Fazio, G. G., Woolaway, J., Blackwell, J., & Brecher, K. 1994, in IAU Symp. 154, Infrared Solar Physics, ed. D. M. Rabin, J. T. Jefferies, & C. Lindsey (Dordrecht: Kluwer), 179
Tritschler, A., Rimmele, T. R., Berukoff, S., et al. 2016, AN, 337, 1064
Warren, H. P., Ugarte-Urra, I., & Landi, E. 2014, ApJS, 213, 11
Wendeln, C., & Landi, E. 2018, ApJ, 856, 28
Wilhelm, K., Curdt, W., Marsch, E., et al. 1995, SoPh, 162, 189
Woods, T. N., Chamberlin, P. C., Harder, J. W., et al. 2009, GeoRL, 36, L01101
Young, P. R., Watanabe, T., Hara, H., & Mariska, J. T. 2009, A&A, 495, 587
Zeeman, P. 1897, Natur, 55, 347
```